CHARACTERIZATION OF TITANIUM-ALUMINIDE ALLOYS FABRICATED USING LASER ENGINEERED NET SHAPING

S.N. Motha[1*], N Maledi[2*] & M. Tlotleng[3]

[1*] Department of Chemical and Metallurgical Engineering, University of the Witwatersrand, South Africa, 378773@students.wits.ac.za

[2] Department of Mechanical Engineering, University of Johannesburg, South Africa, MTlotleng@csir.co.za

ABSTRACT

The continuous study of Ti-Al based alloys has led to the exploration of Laser Engineered Net Shaping (LENS) as a fabrication process alternative to traditional methods such as ingot casting and hot isostatic pressing. However, the fabrication of Ti-Al based alloys using LENS poses various challenges such as post processing thermal cracking, which is caused by a combination of the brittle nature of Ti-Al based alloys and thermal residual stresses. This work investigates the effects of altering LENS parameters on microstructures, microhardness and post processing thermal cracks. The effects of altering LENS parameters on deposition mechanisms were studied by observing changes in the microstructure. The effects of heat treatment on microstructures were also studied. The resulting microstructures and microhardness revealed that Ar gas flow rates lead to slower cooling rates during laser deposition while post heat treatment lead to the reduction in microhardness.

1. INTRODUCTION

There has been a great and growing interest in utilising Ti-Al based alloys as potential replacements for Ni-based superalloys in the aero-engine manufacturing industry. This great interest stems from the unique combination of the material's physical and mechanical properties; which enable high temperature strength as high as that of Ni-based superalloys at half the density [1,2] . The use of Ti-Al based alloys for aero-engine applications has the potential to reduce fuel consumption and increase financial savings in the aviation industry[3]. However, the application of these materials is limited by their imbalance between high temperature creep resistance and ambient temperature ductility. Poor ambient temperature ductility leads to limited processability during manufacturing, This leads to an increase in the production costs when using traditional fabrication methods [4]–[6]. The ambient temperature ductility is attributed to the crystal orientation of γ and α_2+γ phases which are arranged in a Burger's Orientation: $(111)_\gamma$ || $(0001)_\alpha$ and $[110]\gamma||1120]\alpha_2$ [4,5].Numerous attempts have been made to improve the ambient temperature ductility of Ti-Al alloys. These attempts encompass methods such as directional solidification, controlling lamella colony sizes and electromagnetic cold crucible directional solidification [4], [5], [9]. Directional solidification findings established that the maximum attainable ductility of Ti-Al alloys was 20% [6,7]. This value is obtained when the angle between the lamella colony boundaries and the tensile axis is 31° [4], [10], [11]. However, this maximum value of ductility is accompanied by the minimal value of creep strength of close to 0.0 MPa [10], [11]. It was also established that the maximum value of strength (400 MPa) occurs when the angle between lamella boundaries and tensile axis is 90° where ductility is at 0% [4], [10]. The best combination of ductility and strength occurs when lamella colony boundaries are parallel to the tensile axis [4], [10].

Microstructural features which include α_2-α_2 spacing, interplanar spacing and lamella colony sizes have also been adjusted in an attempt to improve ductility [9]. However, in adjusting these microstructural features, it was also established that parameters favourable for the improvement of ductility are detrimental to the creep strength of the α_2+γ structure [6], [11]. Deformation mechanisms which account for ductility can also account for microhardness behaviour of Ti-Al since microhardness is inversely proportional to ductility [12], [13].

Strategies to improve the ductility of Ti-Al alloys have been attempted using traditional fabrication methods such as wrought ingot casting where heat treatment or hot isostatic pressing have been used as post processing methods and have been helpful in studying the evolution of microstructures [14]. These strategies have been successful in the improvement of the ambient temperature ductility, but are extremely costly, tedious and time consuming [15], [16]. In attempt to mitigate shortcomings from these strategies, additive manufacturing (AM) is continuously being investigated as a potential manufacturing process to replace these traditional processes. Laser Engineered Net Shaping (LENS) is an AM process that is able to produce components through a layer upon layer fashion according to a computer aided design. LENS machines, in the manufacturing sectors, are used for the free form fabrication and surface repair of metallic components and have the potential to minimize production costs, time and material wastage during production [15], [16].

LENS comprises of a glove box in which process occurs. The laser and powder deposition head are enclosed in this glove box where processing can occur under oxygen depleted environment so that high purity parts can be produced. Typically, argon is used as both the purge and process gas. To this glove box, two external powder hoppers are attached. The set-up is controlled remotely from a central computer station that is installed an Optomec software. It is from this computer station that slice-files and process input parameters can be manipulated during manufacturing without having to stop and start. YAG laser supplied by (IPG PHOTONICS) is used to melt the depositing powder during manufacturing and is also controlled remotely from the computer station.

Adjusting various process parameters when printing from the LENS system during fabrication can affect the microstructure and mechanical properties of the deposited structure. During

deposition, laser heat input (or energy densities) lead to thermal gradients pile-ups which in turn lead to post process thermal cracking in the build [17], [18]. The crack density and sizes can be influenced by the mechanical behaviour of the material and LENS parameters [17], [18]. This work investigates the effects of altering the Al feed rates and Ar carrier gas flowrates, and using heat treatment, as a post processing step, to transform the resulting microstructure of the manufactured part thereby improving their mechanical properties.

2. EXPERIMENTAL METHODOLOGY

Ti-Al alloys were synthesised on Ti-6Al-4V substrates using the Optmec 850-R LENS machine. The alloys were synthesised from melting, with a laser beam, commercially pure spherical powders of titanium (Ti) and aluminium (Al). Both powders had an average particle size distribution of 45-90 µm. The mixture of Ti and Al powder are displayed in the SEM micrograph in Figure 1. Both Ti and Al powders were supplied by TLS Technik GmbH & Co Spezialpulver, Germany. Scanning Electron Microscope (SEM) micro-image of the feedstock powder is shown in Figure 1.

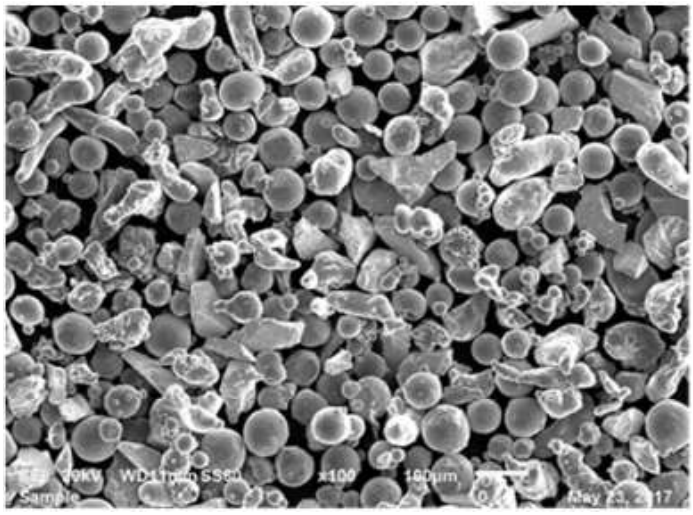

Figure 1: SEM micrograph of Ti and Al powder feed stock (17)

The depositing powders were formed into 1 x 1 x 0.7 cm cubes. The depositing powders were processed from their independent hoppers [Hopper-1: Ti and Hopper-2: Al] and injected into the laser melt-pool that was created on the Ti-6Al-4V base plate and upon cool the molten pool, now a mixture of Ti and Al, form into cube sizes of 1 X 1 X 0.7 cm^3. Argon was used as a carrier gas and shrouded the melt-pool from being oxidised. The powder feed rates can be manipulated to obtain certain compositions (like in functional grade structures, metal matrix composites and so forth) in the printed component. LENS head deposition speed that was used was 1.198 cm/s while the Ti feed rate was kept constant at 2.5 rpm. Al feed rates and Ar carrier gas flowrates were varied as reported in Table 1.

Table 1: LENS parameters used during synthesis of cubes.

Sample number	Al		
	Feed rates (rpm)	**Ar carrier gas flowrates (L/min)**	Power (W)
Ti-Al-2.1	1,5	3	350
Ti-Al-2.2	1,5	4	350
Ti-Al-2.3	1,5	5	350
Ti-Al-2.4	1,5	6	350
Ti-Al-3.1	2	3	350
Ti-Al-3.2	2	4	350
Ti-Al-3.3	2	5	350
Ti-Al-3.4	2	6	350

2.1 Heat treatment

Ti-Al cubes were sectioned in halves for as-built and heat treatment characterisation. Before heat treatment, samples were encapsulated and purged with Ar gas in silica tubes to prevent them from oxidising during heat treatment. Heat treatment was performed in a Nabertherm muffle furnace where the temperature was ramped up to 950°C at heating rate of 3.33°C/s and held for 3 hours before the sample was allowed to cool inside the furnace overnight.

2.1.1 Characterization

In order to understand the characteristics of all the samples, Olympus optical microscope (OM) was used to measure the lengths of the post processing thermal cracks. In addition, SEM with a backscatter diffraction (BSD) mode and Electron High Tension (EHT), was used to study the microstructures of all the samples. Energy Dispersive X-Ray Spectroscopy (EDS/EDX) was used to obtain the chemical compositions of the microstructural features that were observed. Samples were removed from the substrates using diamond wire cutting machine in order to study their phases and lattice parameters using BRUKER D2 PHASER X-ray diffraction (XRD). This XRD used a Cu-Kα (λ=1.54Å) radiation source at a current of 10mA, voltage of 30KV, scan range where 2θ=5° to 90° at a scan speed of 8.5°/min and step increment of 0.026°. Phases were identified using DIFFRAC.EVA V.4.2.2 XRD software. Electron Backscatter Diffraction (EBSD) was used to determine the phase proportions and crystal orientations. The influence of microstructure on mechanical properties was studied by performing microhardness tests were 90 microhardness indentations were made using the Future-Tech Micro hardness Tester Model FM-700, with a load of 500 gf and dwell time of 15 seconds.

3. RESULTS

3.1 Microstructures

Low Al TiAl alloys produced using low Ar carrier gas flowrates (3L/min) produce ß equiaxed dendrites [19] as displayed in Figure 2a. When Ar carrier gas flow rates were increases to 5L/min, an equiaxed α+γ nearly lamellar microstructure was produced as displayed in Figure 2b. Heat treating of the low Al structures lead to an equiaxed $\alpha_2+\gamma$ fully lamellar microstructure [8] which is displayed in Figure 2c. The grain sizes of the heat treated low Al alloys increased with increasing Ar carrier gas flowrates.

High Al alloys produced with low Ar carrier gas flowrates (3L/min) produced α columnar dendrites as displayed in Figure 2d. When Ar carrier gas flowrates were increased to 6L/min, a basket weave α+γ microstructure [20] was produced as displayed in Figure 2e. Heat treating of high Al structures produced uniform γ duplex microstructures [21] as displayed in Figure 2f.

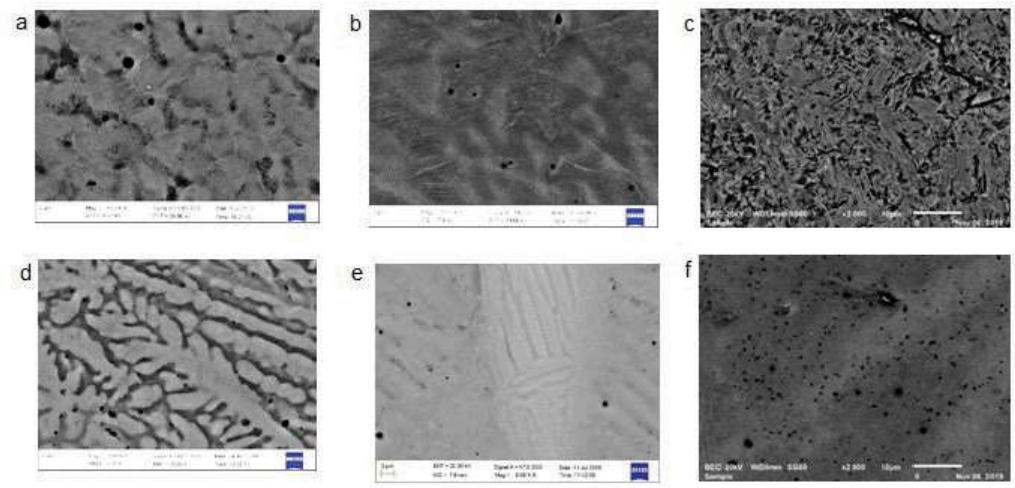

Figure 2: SEM micrographs taken with BSD mode, EHT set at 20.0kV illustrating microstructures of samples: (a)as produced with Low Al feed rate (1.0rpm)- 42.71at%Al57.29at%Ti and low Ar carrier gas flowrate (3L/min) (b) as produced with low Al feed rate (1.0rpm) -56.02at%Al43.98at%Ti and high Ar carrier gas flowrates (5L/min) (c) heat treated TiAl alloy produced with low Al feed rate (1.0rpm) (d) as produced with high Al feed rate (2.0rpm) - 48.17at%Al51.83at%Ti and low Ar carrier gas flow rate (3L/min) (e) as produced with high Al feed rate (2.0rpm)- 63.22at%Al36.78at%Ti and high Ar carrier gas flow rate (5L/min) (f) heat treated TiAl alloys produced with high Al feed rate (2.0rpm)

3.2 Microhardness

Microhardness values for samples generated at low Al feed rate (1.5 rpm) range from 509,056HV to 535,556HV with an average of 523,792HV. These values are wavy (up and down) with the lowest and highest HV value reported for 3 l/min and 6 l/min, respectively. Microhardness values drop when Al feed rates were increased to 2.0 rpm for the same Ar gas flowrate. In fact a significant drop in HV values was achieved for the sample that was produced with hardness was achieved for 4 l/min and was followed with a sharp rise in hardness value with an increase in Ar flowrate. Microhardness values at high Al feed rates drop to values within a range of 464,056HV to 498,889HV and averaged 476,24HV. These was attributed to the difference in the as-produced microstructures. Equiaxed dendritic and nearly lamellar microstructures seemed to be yielding higher microhardness values when compared to microstructures containing columnar dendrites, basket weave structure and fully lamellar equiaxed grain.

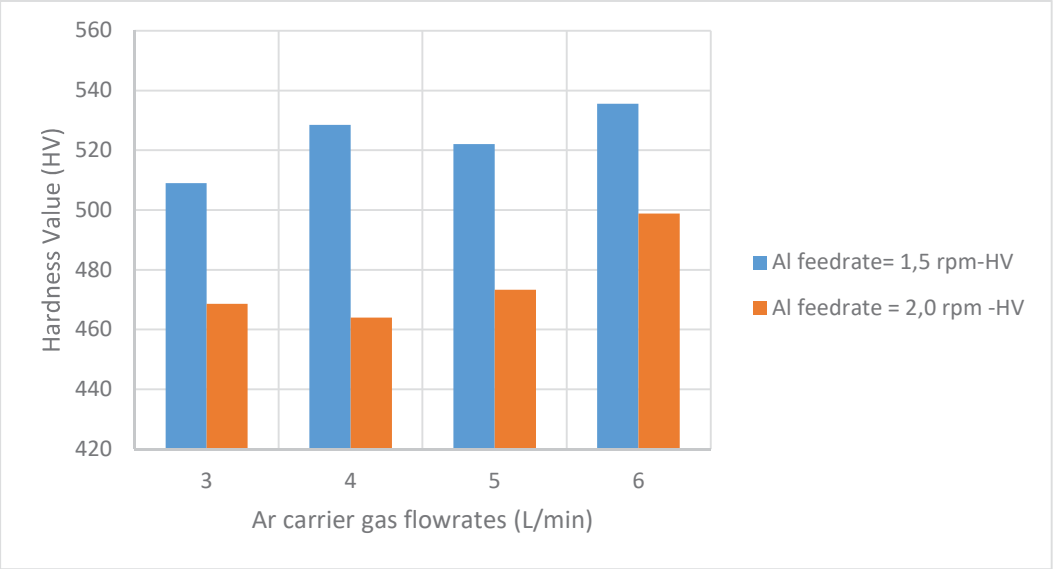

Figure 3: Graphical representation of the effect of Al feed rates and Ar carrier gas flowrates on microhardness of as produced TiAl alloys

The micro-hardness values of heat treated Ti-Al samples dropped significantly compared to the as produced alloys as observed in the bar graph illustrated in Figure 4. The microhardness profiles are also wavy. Micro-hardness values of heat treated Ti-Al alloys produced with low Al feed rate (1.5 rpm) dropped to a range from 387 HV to 448 HV and an average of 408 HV. The maximum hardness for these heat treated structures achieved was 447,53HV at 5L/min and the minimum was 386,74HV at 4L/min. It was observed that micro-hardness values increase with grain sizes. Micro-hardness values of heat treated Ti-Al samples produced with Al feed rate of 2.0rpm dropped to a range from 304 HV to 334 HV and an average hardness of 315 HV. The maximum hardness value achieved for these structures was 334,34HV at 6L/min and the minimum value of 304,13HV at 4L/min. This indicates that microstructures that contain the γ-phase yield low hardness.

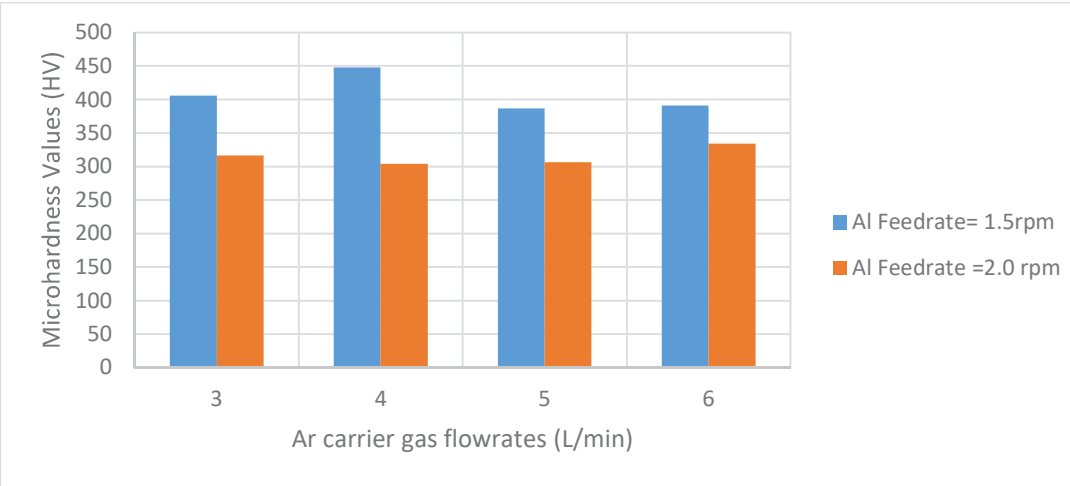

Figure 4: Microhardness of Heat treated TiAl alloys

3.3 Crystal structure

Since as produced and heat treated TiAl 2.3 sample number had the lowest crack density and lengths among all samples studied, further investigations regarding their behaviour was carried out by performing XRD. XRD confirmed the presence of γ phase with a [1 1 1] close packed plane as can be observed in Figure 5 alongside Table 2. It is observed that the as produced TiAl 2.3 sample number had XRD peaks from crystallographic planes that include [1 1 1]$_\gamma$, [2 2 0]$_\gamma$ and [2 1 1]$_\beta$. The d-spacing d(Å) of the close packed planes [1 1 1] was calculated to have had increased from 2.139Å to 2.517Å and the lattice parameter increased from 3.705A to 4.359A during heat treatment. The XRD peaks from different crystallographic planes which include [2 0 0]$_\gamma$, [2 1 0]$_\alpha$, [3 2 0]$_\alpha$ and [3 2 1]$_\beta$ were detected on heat treated samples. These peaks revealed various d-spacings and lattice parameter as observed in Table 2. Heat treatment also led to the broadening of the peaks which indicated strain distribution according to Stephen's Model [22]. Bragg's Equation for diffraction was used to calculate lattice parameters $n\lambda_{Cu\,K\alpha} = 2 * d_{[hkl]} sin\theta_{(hkl)}^{BRAGG}$ [23].

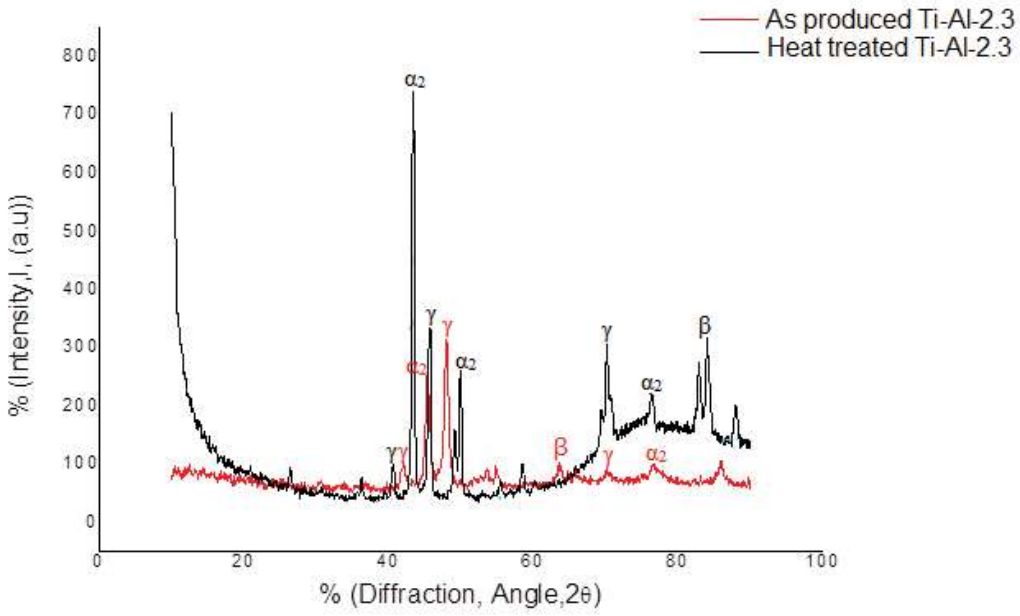

Figure 5: XRD patterns (a) As produced and heat treated TiAl-2.3

Table 2: XRD peaks and lattice parameters calculated

2θ(˚)-peaks	Miller Indices [h k l]	Crystal structure/ Reflections present	$d(\text{Å}) = \frac{\lambda_{Cu\,K\alpha}}{2 * sin\theta}$	$a = d_{hkl} * \sqrt{h^2 + k^2 + l^2}$	Phase
42.199	[1 1 1]	FCC	2.139	3.705	γ
45.420	-	HCP	-	-	α_2
48.088	[2 2 0]	FCC	1.889	3.779	γ
63.540	[2 1 1]	BCC	1.462	3.582	β
70.196	[2 2 0]	FCC	1.340	3.787	γ
Heat treated					
35.626	[1 1 1]	FCC	2.517	4.359	γ

38.420	-	HCP	-	-	α_2
40.687	[2 0 0]	FCC	2.215	4.429	γ
44.113	-	HCP	-	-	α_2
44.956	[2 1 0]	HCP	2.014	4.503	α_2
77,689	[3 2 0]	HCP	1.227	4.426	α_2
82,723	[3 2 1]	BCC	1.165	4.348	β
82,986	[3 2 1]	BCC	1.162	4.359	β

Figure 6 shows that post processing thermal crack lengths of heat treated samples were longer than the as produced samples. In the as produced state (Figure 6a), crack lengths have an average of *23.165 x10^{-6} m*. The crack length in the heat treated state (Figure 6b) had an average crack length of *35.208 x10^{-6} m*.

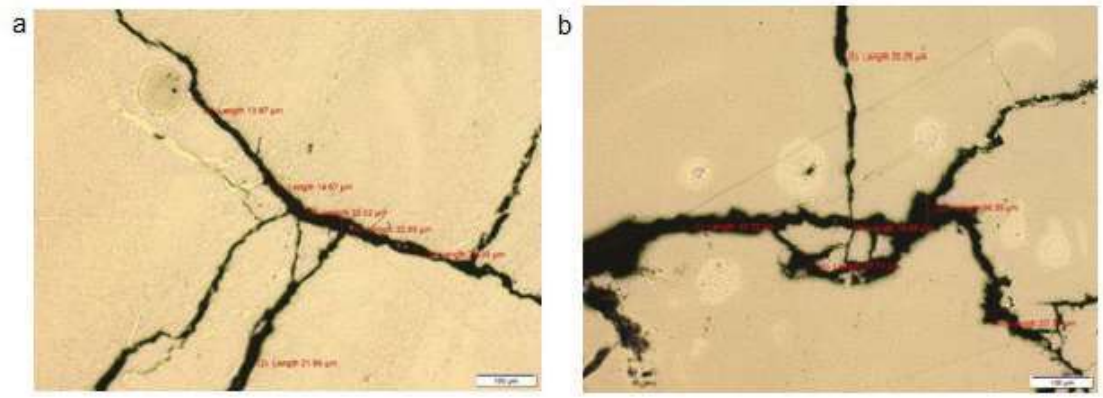

Figure 6: (a) Average crack length of as a produced TiAl 2.3: 23.165 x10^{-6} m (b) Average crack length of heat treated TiAl 2.3: 35.208 x10^{-6} m

The EBSD performed revealed the basket weave nature of TiAl-2.3 sample are primary and secondary basket weaves and were mostly comprised of the hexagonal close packed (HCP) α phase as displayed in colour coded image in Figure 7a. These HCP crystals have various orientations with respect to the z-axis as can be observed in the Inverse Polar Figure displayed in Figure 7b. The matrix phase is believed to be γ. But since the software used to identify the crystal orientations does not have FCC-γ in its databases, the solution does not appear on the images in colour codes.

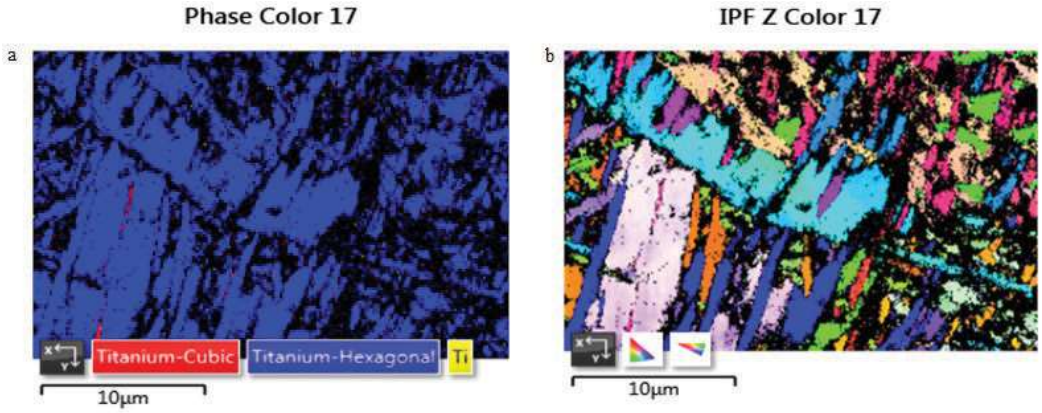

Figure 7: (a) Colour coded EBSD image of as produced TiAl 2.3 (b) EBSD inverse pole figure (IPF) displaying crystal orientation map for as produced Ti-Al-2.3

3. DISCUSSION

Inert gases such as Ar and He conserves thermal energy [25], [26]. This conservation of heat energy is influenced by Ar gas conductivity which enhances higher ratios of convective heat transfer of Ar gas to radiative heat transfer at melt free solidified surfaces during laser deposition [27]. This enables higher radiative heat transfer to melt free surface which enable solid state phase reactions [8] on melt free surface post laser deposition. This leads to the formation of nearly lamellar and fully lamella microstructures which form through solid state phase transformation reactions [7]. As Ar gas flow rates increase, it becomes easier to blow the gas on the solid melt free surface, which increases heat transfer ratios [27].

At low Al concentrations (45 – 49 at.% Al), solidification takes place through recrystallization of the ß dendrites from the melt, followed by the peritectic formation of α phase upon cooling [19], [28] cooling. The development of these microstructures as Ar gas flow rates are increased are evident in microstructures observed in as produced state as Ar gas flow rates were increased. These microstructures provide evidence that increasing Ar gas flow rates allow peritectic phase reaction: $\beta \rightarrow \beta + \alpha \rightarrow \alpha$ where α plates are formed and while Ti segregates to remaining ß ribs [20]. As Ar flow rates are increased further, γ lamellae precipitate within α plates forming α+γ nearly lamellar or basket weave structure through the following solid state phase transformation reactions: $\alpha \rightarrow \alpha + \gamma$ [19], [20].

At higher Al concentrations above 49 at.% Al, α columnar dendrites recrystalize from molten [19] during solidification which occurs post laser deposition. This microstructure later transforms into the γ phase due to annealing at 950°C [8], [21]. This is a result of solid state phase transformation reactions which occur due to heating ($\alpha \rightarrow \alpha + \gamma \rightarrow \alpha_2 + \gamma$), and leads to fully lamellar equiaxed microstructure [19]. These microstructural developments are observed as Ar flow rates are increased. This confirms that increasing Ar gas volumetric flow rates allow for solid state transformation reactions which produce equiaxed granular structures [20] and enhances the production of γ phase.

Heat treating at 950°C causes low Al concentration builds to produce fully lamellar α_2+γ microstructures [7], while higher Al concentrations (>49 at.% Al) produce uniform duplex γ fine grained microstructures [3]. According to Schuster and Palm [28], phases produced during heat treatment are generally thermodynamically favourable at 950°C [28].

At low Al feed rate as Ar carrier gas flow rates were increased during production, the equiaxed microstructure appeared coarser in the heat treated state. This indicates a reduction in cooling rates as Ar flow rates are increased since grain growth and coarsening is enhanced by slower cooling rates [29].

Heat treatment also lead to the increase in interplanar spacing and reduced microhardness values. This could be attributed to thermal stress relief due to heat treatment [30] which softens the material and reduces microhardness values during the annealing process [31]. The increase in interplanar spacings can be attributed to the ability of heat treatment to increase diffusion rates of both Ti and Al [32]. Faster diffusion rates lead to reduced lattice constant c/a [32], [33], since diffusion rates increases during heat treatment. Lattice constants such as c/a ratio are affected by thermal expansion which expands the lattice at higher temperatures during heat treatment [34] , which can account for the increase in interplanar spacings and lattice parameter a. Thermal expansion also accounts for increased crack lengths post heat treatment. However, the nature of post processing thermal cracks can also be accounted by the general fracture behaviour of the material [18], [24] such as strength and ductility.

The $\alpha_2+\gamma$ phase has higher microhardness than the uniform γ-phase [35]. The uniform γ-phase microstructures have significantly lower microhardness due to the absence of α_2 phase [36]. However, uniform γ had a higher number of post processing thermal cracks than $\alpha_2+\gamma$ since thermal cracks were initiated at γ phase and propagated rapidly in a cleavage fashion through the microstructure. While in two phase $\alpha_2+\gamma$ microstructure, α_2 which is harder and serves as crack initiation sites and prevent rapid crack propagation during thermal strain. These two phase microstructures allow cracks to propagate on α_2 in a ligament fashion, hindering rapid crack propagation during thermal stress to which materials are subjected [9].

4. CONCLUSIONS

From the analysis of all experimental work performed, it was concluded that higher Ar carrier gas flowrates led to slower cooling rates. It was also established that Al is a γ phase stabiliser. Based on XRD findings, it can be concluded that heat treatment induced thermal expansion in the material leading therefore to an increase in the interplanar spacing and thermal crack lengths. Reduction in microhardness values are due to stress relief during heat treatment.

REFERENCES

[1] **T. J. Kelly, M. J. Weimer, C. M. Austin, B. London, D. E. Larson Jr, and D. A. Wheeler**, 'Heat treatment of gamma titanium aluminide alloys', May 2001.

[2] **J. C. Chesnutt**, 'GE Aircraft Engines One Neumann Way', pp. 45212–6301, 1992.

[3] **Y.-W. Kim**, 'Ordered intermetallic alloys, part III: gamma titanium aluminides', *Jom*, vol. 46, no. 7, pp. 30–39, 1994.

[4] **H. Zhang, X. Tang, C. Zhou, H. Zhang, and S. Zhang**, 'Comparison of directional solidification of γ-TiAl alloys in conventional Al2O3 and novel Y2O3-coated Al2O3 crucibles', *Journal of the European ceramic society*, vol. 33, no. 5, pp. 925–934, 2013.

[5] **M. Kim, M. Oh, J. Lee, H. Inui, M. Yamaguchi, and D.-M. Wee**, 'Composition and growth rate effects in directionally solidified TiAl alloys', *Materials Science and Engineering: A*, vol. 239, pp. 570–576, 1997.

[6] **Y.-W. Kim, W. Smarsly, J. Lin, D. Dimiduk, and F. Appel**, *Gamma Titanium Aluminide Alloys 2014: A Collection of Research on Innovation and Commercialization of Gamma Alloy Technology*. John Wiley & Sons, 2014.

[7] **F. Appel**, 'TiAl Intermetallics', *Encyclopedia of Aerospace Engineering*, 2010.

[8] **F. Appel, J. D. H. Paul, and M. Oehring**, *Gamma titanium aluminide alloys*. Wiley Online Library, 2011.

[9] **S.-W. Kim, Y.-S. Na, J.-T. Yeom, S. E. Kim, and Y. S. Choi**, 'An in-situ transmission electron microscopy study on room temperature ductility of TiAl alloys with fully lamellar microstructure', *Materials Science and Engineering: A*, vol. 589, pp. 140–145, 2014.

[10] **M. Yamaguchi, D. Johnson, H. Lee, and H. Inui**, 'Directional solidification of TiAl-base alloys', *Intermetallics*, vol. 8, no. 5–6, pp. 511–517, 2000.

[11] **Z. Jiao, J. Luan, and C. Liu**, 'Strategies for improving ductility of ordered intermetallics', *Progress in Natural Science: Materials International*, vol. 26, no. 1, pp. 1–12, 2016.
[12] **J. Cahoon, W. Broughton, and A. Kutzak**, 'The determination of yield strength from hardness measurements', *Metallurgical transactions*, vol. 2, no. 7, pp. 1979–1983, 1971.
[13] **S. C. Krishna, N. K. Gangwar, A. K. Jha, and B. Pant**, 'On the prediction of strength from hardness for copper alloys', *J. Mater*, vol. 2013, pp. 1–6, 2013.
[14] **H. Clemens *et al.***, 'Grain refinement in γ-TiAl-based alloys by solid state phase transformations', *Intermetallics*, vol. 14, no. 12, pp. 1380–1385, 2006.
[15] **M. Griffith, D. Keicher, and C. L. Atwood**, 'Free form fabrication of metallic components using laser engineered net shaping (LENS {trademark})', Sandia National Labs., Albuquerque, NM (United States), 1996.
[16] **D. Gu**, *Laser additive manufacturing of high-performance materials*. Springer, 2015.
[17] **W. Liu and J. DuPont**, 'Fabrication of Titanium Aluminide Matrix Composites by Laser Engineered Net Shaping 124', presented at the 2002 International Solid Freeform Fabrication Symposium, 2002.
[18] **A. Sharman, J. Hughes, and K. Ridgway**, 'Characterisation of titanium aluminide components manufactured by laser metal deposition', *Intermetallics*, vol. 93, pp. 89–92, 2018.
[19] **C. McCullough, J. Valencia, C. Levi, and R. Mehrabian**, 'Phase equilibria and solidification in Ti-Al alloys', *Acta Metallurgica*, vol. 37, no. 5, pp. 1321–1336, 1989.
[20] **V. Küstner *et al.***, 'Gamma titanium aluminides 2003', 2003.
[21] **Y.-W. Kim and D. M. Dimiduk**, 'Progress in the understanding of gamma titanium aluminides', *Jom*, vol. 43, no. 8, pp. 40–47, 1991.
[22] **P. W. Stephens**, 'Phenomenological model of anisotropic peak broadening in powder diffraction', *Journal of Applied Crystallography*, vol. 32, no. 2, pp. 281–289, 1999.
[23] **S. O. Kasap**, *Principles of electronic materials and devices*. Tata McGraw-Hill, 2006.
[24] W. E. Voice, M. Henderson, E. F. Shelton, and X. Wu, 'Gamma titanium aluminide, TNB', *Intermetallics*, vol. 13, no. 9, pp. 959–964, 2005.
[25] **A. Traidia, F. Roger, A. Chidley, J. Schroeder, and T. Marlaud**, 'Effect of helium-argon mixtures on the heat transfer and fluid flow in gas tungsten arc welding', *Journal of Chemistry and Chemical Engineering*, vol. 5, no. 9, pp. 854–861, 2011.
[26] **Y. Ogino and Y. Hirata**, 'Numerical simulation of metal transfer in argon gas-shielded GMAW', *Welding in the World*, vol. 59, no. 4, pp. 465–473, 2015.
[27] **Z. Li, L. Liu, W. Ma, and K. Kakimoto**, 'Effects of argon flow on heat transfer in a directional solidification process for silicon solar cells', *Journal of Crystal Growth*, vol. 318, no. 1, pp. 298–303, 2011.
[28] **J. C. Schuster and M. Palm**, 'Reassessment of the binary aluminum-titanium phase diagram', *Journal of phase equilibria and diffusion*, vol. 27, no. 3, pp. 255–277, 2006.
[29] **F. Gil, M. Ginebra, J. Manero, and J. Planell**, 'Formation of α-Widmanstätten structure: effects of grain size and cooling rate on the Widmanstätten morphologies and on the mechanical properties in Ti6Al4V alloy', *Journal of Alloys and Compounds*, vol. 329, no. 1–2, pp. 142–152, 2001.
[30] **F. Bassani**, *Encyclopedia of condensed matter physics*. Elsevier acad. press, 2005.
[31] **S. Hashmi**, *Comprehensive materials finishing*. Elsevier, 2016.
[32] **I. Polmear, D. StJohn, J.-F. Nie, and M. Qian**, *Light alloys: metallurgy of the light metals*. Butterworth-Heinemann, 2017.
[33] **C. Suryanarayana and M. G. Norton**, 'Crystal structure determination. II: hexagonal structures', in *X-Ray Diffraction*, Springer, 1998, pp. 125–152.
[34] **J. Elmer, T. Palmer, S. Babu, and E. Specht**, 'In situ observations of lattice expansion and transformation rates of α and ß phases in Ti–6Al–4V', *Materials Science and Engineering: A*, vol. 391, no. 1–2, pp. 104–113, 2005.
[35] **S. Gebhard, F. Pyczak, and M. Göken**, 'Microstructural and micromechanical characterisation of TiAl alloys using atomic force microscopy and nanoindentation', *Materials Science and Engineering: A*, vol. 523, no. 1–2, pp. 235–241, 2009.

[36] **J. Kuang, R. Harding, and J. Campbell**, 'Microstructures and properties of investment castings of γ-titanium aluminide', *Materials Science and Engineering: A*, vol. 329, pp. 31–37, 2002.